47th AIAA Aerospace Sciences Meeting Including The New Horizons Forum and Aerospace Exposition
5 - 8 January 2009, Orlando, Florida

AIAA 2009-273

A Computational Study of the Aerodynamics and Aeroacoustics of a Flatback Airfoil Using Hybrid RANS-LES

Christopher Stone*
Computational Science & Engineering, Athens, GA, 30606, USA
Matthew Barone†
Sandia National Laboratories, Albuquerque, NM, 87185-1124, USA
C. Eric Lynch‡ and Marilyn J. Smith§
Georgia Institute of Technology, Atlanta, Georgia, 30332-0150, USA

This work compares the aerodynamic and aeroacoustic predictions for flatback airfoil geometries obtained by applying advanced turbulence modeling simulation techniques within Computational Fluid Dynamics (CFD) methods that resolve the Reynolds-Averaged Navier-Stokes (RANS) equations of motion. These flatback airfoil geometries are designed for wind turbine applications. Results from different CFD codes using hybrid RANS-LES and RANS turbulence simulations are correlated and include analysis with experimental data. These data comparisons include aerodynamic and a limited amount of aeroacoustic results. While the mean lift prediction remains relatively insensitive across many simulation techniques and parameters, the mean drag prediction is dependent on both the grid and turbulence simulation method. Aeroacoustic predictions obtained from post-processing of the airfoil surface pressure agree reasonably well with experimental data when consistent boundary layer tripping is used for both the simulation and experimental configuration.

Nomenclature

a	Speed of sound
c	Chord, m
C_d	Sectional drag coefficient
C_D	Total drag coefficient
C_l	Sectional lift coefficient
C_L	Total lift coefficient
c_p	Specific heat due to constant pressure
C_p	Pressure coefficient
d	Distance to the wall
e	Specific internal energy
f	Frequency of vortex shedding, 1/s
h	Base length of the flatback airfoil trailing edge, m or enthalpy
i, j, k	Unit vectors in the x,y,z directions

*President and Chief Scientist, AIAA Member.
†Senior Member of Technical Staff, Wind Energy Technology Dept., AIAA Senior Member.
‡Ph.D. Student and Graduate Research Assistant, School of Aerospace Engineering, AIAA Student Member.
§Associate Professor, School of Aerospace Engineering, AIAA Associate Fellow.

k	Turbulent kinetic energy
l	Length
M	Mach number
N	Number of grid points
p	Pressure
Pr_L	Laminar Prandtl number, $Pr_L = c_p\mu/\kappa$
q	Heat flux vector
R	Distance from sound source to observer, m
R_{LL}	Lift fluctuation correlation function
Re	Reynolds number
St	Strouhal number, $St = fh/U_\infty$
t	Time, s
T	Temperature
u, v, w	Velocity in the x, y, z directions
x, y, z	Cartesian coordinate system in the stream, normal and span directions
Z	Spanwise extent of the computational domain
y^+	Dimensionless sublayer-scaled distance, $u_T y/\nu$
U	Velocity
α	Angle of attack, degrees ($^\circ$)
Δ	Local grid cell size or change in quantity
λ	Acoustic wavelength
μ	Molecular viscosity
μ_T	Eddy viscosity
Λ	Spanwise lift correlation length
ω	vorticity
ρ	Density
σ	centroid of correlation function
τ_{ij}	Reynolds shear stress tensor
θ	Angle, as defined in text
ω	Vorticity

Subscripts and Superscripts

i, j, k	Tensor directions
l	Length
rms	Root mean square
sgs	Subgrid-scale
tot	Total
T	Turbulent
$(.)'$	Fluctuating term for a time-averaged quantity
$(.)''$	Fluctuating term for a Favre-averaged quantity
$\overline{(.)}$	Mean quantity
$\widetilde{(.)}$	Mass-averaged quantity
∞	Free stream

Abbreviations

CFD	Computational Fluid Dynamics
DES	Detached Eddy Simulation
GT–HRLES	Georgia Tech hybrid RANS/LES turbulence method
HRLES	Hybrid RANS/LES
LES	Large Eddy Simulation
RANS	Reynolds-Averaged Navier-Stokes

SA	Spalart-Allmaras RANS turbulence model
SPL	Sound pressure level, dB (ref: 20×10^{-6} Pa)

I. Introduction

A specific barrier to widespread wind turbine deployment, especially in densely populated areas, is the high level of flow-generated noise. To ensure that wind energy can attain appreciable deployment in such areas, *aeroacoustic* (i.e., aerodynamically generated) noise must be reduced,[1–3] while maintaining optimal turbine performance. The achievement of these two technical goals will permit the expansion and new development of wind power resources in areas near population centers.

The problems of maintaining or improving performance while reducing the aeroacoustic noise cannot be tackled as separate goals, as they are inherently coupled. For example, the design of quieter turbines could permit higher turbine tip-speeds, which in turn can improve performance. There are many different sources of aeroacoustic noise in a full-scale wind turbine configuration, which are driven by the unsteady aerodynamic flow field. For utility-scale wind turbines, (1) turbulent inflow noise, (2) turbulent boundary layer trailing edge noise and (3) blunt trailing edge vortex shedding noise are the primary sources of aerodynamic noise. Turbulent inflow noise is due to turbulent flow/leading-edge interaction, while turbulent boundary layer trailing edge noise is due to scattering of fluctuations in the turbulent boundary layer by the trailing edge. Blunt trailing edge vortex is a narrow-band noise source that results from organized shedding of vorticity in the wake of a blunt trailing edge. It is clear that accurate characterization of the local unsteady aerodynamic flow field is key to predicting, understanding, and ultimately reducing the aeroacoustic noise.

With respect to the performance goals, it is well known that the power generating potential of a given turbine increases proportionately with the rotor disk area. To this end, designers have been investigating new wind turbine configurations with ever longer blades. To reduce the overall rotor weight and the resulting drive-train stress associated with these longer blades, light-weight, composite airfoils are being deployed. To maintain the necessary structural integrity and longevity, airfoils with trailing edges that are significantly thickened or even blunted have been studied.[4,5] The complex, bluff-body nature of these airfoils, commonly known as *flatback* airfoils due to their trailing-edge shape, comes with penalties including increased drag and aeroacoustic noise. Recently, Berg and Zayas[6] investigated both the aeroacoustic noise and aerodynamic performance of a flatback airfoil design in a series of anechoic wind-tunnel experiments. Similar performance studies of flatback airfoils have also been investigated experimentally and numerically.[4,7] Low-fidelity (potential) aerodynamic models are not adequate to properly predict the strength and location salient aerodynamic phenomena for these wind-turbine airfoils. Existing empirical estimates[8] for the noise generation do not account for thicknesses greater then 1% of chord, complicating the design of new wind turbines.

Computational fluid dynamic (CFD) modeling of wind turbines is desirable as a design and research tool for both conventional as well as these flatback airfoils, but it is limited because of the difficulties encountered in accurately predicting the aerodynamic flow field features (e.g., turbulent inflow, separation) that are key to the performance and noise predictions. Wind turbines routinely operate at a wide disparity of local Reynolds numbers (Re) that can reach values of $Re > 10^7$ near the rotor tips. The ratio of the largest-to-smallest turbulence scales is proportional to $Re^{9/2}$. As a consequence, a fully-resolved simulation (e.g., *Direct Numerical Simulations* (DNS)) for design and analysis of wind turbines (or even the airfoils) is not practical for the foreseeable future, without the aid of massively parallel computational hardware. To reduce the computational costs, attempts are made to statistically model the effects of these turbulent scales, while numerically simulating the mean flow field. The turbulence models are *tuned* utilizing a number of different classic test cases, none of which include the unsteady, rotational configurations found in wind turbines. This traditional method, CFD or Reynolds Averaged Navier-Stokes (RANS) CFD, applies these empirical models to all turbulence length- and time-scales, resulting in a steady-state prediction of the macroscopic flow field. Under specific time-scale conditions, an unsteady solution for the slowest time-scales (URANS) is possible. Despite their wide usage, these models are overly dissipative and are poorly suited for predicting unsteady, separated flow typically encountered at high wind speeds (i.e., high angle-of-attack) and near the rotor

hub (bluff-body)[9–11] where viscous-induced separation is dominant. Furthermore, due to their steady-state nature, direct acoustic predictions derived from RANS are questionable. These restrictions considerably limit RANS's predictive potential for wind turbine design and analysis.

Large-Eddy Simulation (LES) methods are an alternative technique to RANS and DNS. Unlike RANS, LES exactly simulates the larger, energy-containing length scales and reverts to phenomenological/empirical modeling only at length-scales smaller then the local grid resolution.[12,13] By directly resolving the most energetic eddies in both time and space, LES can capture the unsteadiness found in separated flows more realistically. However, for LES to be applicable, the grid resolution must be sufficiently refined so that its scaling cut-off will capture eddies in the *inertial* sub-range. In this regime, the turbulence statistics are considered more *universal* and less dependent on the geometry of the flow.[14,15] Unfortunately, the inertial sub-range requirement makes LES an expensive albeit tractable (with sufficient parallel processing) simulation method.

Unfortunately, the flow around a wind turbine has an extremely high Reynolds number (typically, on the order of several millions) and is geometrically complex (e.g., rotating turbine with twisted blades). Even with the computational savings offered by LES, the effective cost remains far too high for design-level CFD studies. As a compromise, hybrid modeling approaches combine near-wall RANS models with LES methods where the turbulent eddy scale disparities are less severe. This methodology can be implemented in existing LES and RANS codes. Most engineering-based applications typically modify an existing RANS code so that it will employ the LES model in separated flow regions. One of the first, and most commonly used hybrid approach is Detached-Eddy Simulation (DES).[12,16] In this approach, the Spalart-Allmaras one-equation or $\kappa - \omega$ SST RANS model is used in wall-bounded regions and then transitions to a Smagorinsky[17] eddy-viscosity model.

In the remainder of this work, a series of numerical simulations mimics some selected configurations of the experiments conducted with a flatback version of the DU97-W-300 airfoil reported in.[6,18] These numerical simulations are conducted using different existing RANS CFD codes with two hybrid RANS-LES turbulence simulation methods. These results are correlated with aerodynamic loads (e.g., integrated lift and drag forces) and turbulence statistics in the wake. The simulated turbulence data are used to estimate the blunt trailing edge vortex-shedding noise and compared to the experimental acoustic measurements of the vortex-shedding tone.

II. Hybrid RANS/LES Turbulence Simulation Techniques

Recent research efforts[19,20] indicate that advanced turbulence simulation techniques in the guise of hybrid RANS/LES methods show some promise in bridging the gap between RANS and LES computational techniques. It has been postulated[19] that hybrid techniques in legacy CFD codes should capture the largest scales wherever grid resolution is sufficient to support LES. Thus even coarse grids, more suitable for *Very-Large LES* (VLES), should be more representative of the flow physics than RANS simulations on comparably-sized grids.

The compressible Navier-Stokes equations, when Favre-averaged (mass-averaged), can be mathematically expressed as :

$$\frac{\partial \overline{\rho}}{\partial t} + \frac{\partial}{\partial x_j}(\overline{\rho}\widetilde{u_j}) = 0$$

$$\frac{\partial}{\partial t}(\overline{\rho}\widetilde{u_i}) + \frac{\partial}{\partial x_j}(\overline{\rho}\widetilde{u_i}\widetilde{u_j}) = -\frac{\partial \overline{p}}{\partial x_i} + \frac{\partial \overline{\sigma_{ij}}}{\partial x_j} - \frac{\partial}{\partial x_j}(\overline{\rho u_i'' u_j''})$$

$$\begin{aligned}\frac{\partial}{\partial t}[\overline{\rho}(\widetilde{e} + 0.5\widetilde{u_i}\widetilde{u_i})] + \frac{\partial}{\partial x_j}[\overline{\rho}\widetilde{u_j}(\widetilde{h} + 0.5\widetilde{u_i}\widetilde{u_i})] &= \frac{\partial}{\partial x_j}(-q_{L_j} + \widetilde{u_i}\overline{\sigma_{ij}}) - \frac{\partial}{\partial t}[0.5\overline{\rho u_i'' u_i''}] \\ &+ \frac{\partial}{\partial x_j}[-\widetilde{u_j}\overline{\rho u_i'' u_j''} + \widetilde{u_j}0.5\overline{\rho u_i'' u_i''} - \overline{\rho u_j'' h''} \\ &+ \overline{\sigma_{ji} u_i''} - 0.5\overline{\rho u_j'' u_i'' u_i''}]] \end{aligned} \quad (1)$$

As a result of the averaging process, a Reynolds-stress tensor ($\overline{\rho}\tau_{ij} = -\overline{\rho u_i'' u_i''}$) appears that requires closure. The turbulent kinetic energy (k) can then be defined as $\overline{\rho}k = 0.5\overline{\rho u_i'' u_i''}$. Favre-averaging also gives rise to the the turbulent heat flux ($q_{Ti} = \overline{\rho u_i'' h''}$) and the rate of turbulent dissipation ($\overline{\rho}\epsilon = \overline{\sigma_{ji}\frac{\partial u_i''}{\partial x_j}}$). For flows up through the low supersonic regime, the molecular diffusion and turbulent transport terms ($\overline{\sigma_{ji} u_i''} - \overline{\rho u_j'' 0.5 u_i'' u_i''}$) are typically ignored.[21]

$$\frac{\partial \overline{\rho}}{\partial t} + \frac{\partial}{\partial x_j}(\overline{\rho}\widetilde{u_j}) = 0$$

$$\frac{\partial}{\partial t}(\overline{\rho}\widetilde{u_i}) + \frac{\partial}{\partial x_j}(\overline{\rho}\widetilde{u_i}\widetilde{u_j}) = -\frac{\partial \overline{p}}{\partial x_i} + \frac{\partial \overline{\sigma_{ij}}}{\partial x_j} - \frac{\partial}{\partial x_j}(\overline{\rho}\tau_{ij})$$

$$\begin{aligned}\frac{\partial}{\partial t}[\overline{\rho}(\widetilde{e} + 0.5\widetilde{u_i}\widetilde{u_i})] + \frac{\partial}{\partial x_j}[\overline{\rho}\widetilde{u_j}(\widetilde{h} + 0.5\widetilde{u_i}\widetilde{u_i})] &= \frac{\partial}{\partial x_j}(-q_{L_j} + \widetilde{u_i}\overline{\sigma_{ij}}) - \frac{\partial}{\partial t}[\overline{\rho}k] \\ &+ \frac{\partial}{\partial x_j}[-\widetilde{u_j}\overline{\rho}\tau_{ij} + \widetilde{u_j}\overline{\rho}k - q_{T_j}] \end{aligned} \quad (2)$$

If symmetry is assumed, the Reynolds-stress tensor yields six unknowns that are approximated using models about the behavior of the fluctuating correlations, $\overline{u_i'' u_j''}$. These approximations yield the set of RANS turbulence models, ranging from algebraic to two-equation techniques. It was previously noted that the current practice is to assume the Boussinesq approximation, which can be utilized to relate the fluctuations to an eddy viscosity, μ_T:

$$\overline{\rho}\tau_{ij} = 2\mu_T[S_{ij} - \frac{1}{3}\frac{\partial \widetilde{u_k}}{\partial x_k}\delta_{ij}] - \frac{2}{3}\overline{\rho}k\delta_{ij} \quad (3)$$

Similarly, the turbulent heat flux vector can be related to the eddy viscosity, μ_T, via proportionality to the mean temperature gradient:

$$q_{Ti} = -\frac{\mu_T}{Pr_T}\frac{\partial \widetilde{h}}{\partial \widetilde{x_j}} = -\frac{\mu_T c_p}{Pr_T}\frac{\partial \widetilde{T}}{\partial \widetilde{x_j}} \quad (4)$$

that introduces the turbulent Prandtl number, Pr_T, which can be either constant or variable, depending on the application. Finally, the rate of turbulent dissipation can be expressed as

$$\overline{\rho}\epsilon = \overline{\mu[2S_{ji}S_{ij}'' - \frac{2}{3}u_{kk}u_{ii}'']} \quad (5)$$

As previously discussed, LES directly captures the large turbulence eddies as part of the solution of the Favre-averaged Navier-Stokes equations, relegating the smaller turbulence eddies to be modeled. In order to separate these effects, in addition to the averaging process, the variables in the equation of motion should

also be filtered (typically referred to as Favre-filtering) to obtain the small or subgrid scale (sgs) turbulence. These filtering techniques are discussed in Wilcox.[21]

The hybrid RANS/LES methods are developed by computing these closure quantities for both RANS and LES, and then combining them via either zonal and blended approaches. In the zonal approach, the RANS model provides the near-wall model and the matching interface with the outer LES simulation is defined arbitrarily *a priori* to the simulation. In the blended approach, the hybrid simulation smoothly combines compatible forms of the LES and RANS equations, again using the RANS model to resolve the near-wall flow. Here, a blending function smoothly combines the RANS turbulent kinetic energy and subgrid kinetic energy.

Two blended RANS/LES approaches were applied in this paper: DES and GT–HRLES. A short description of both is provided, along with seminal references, for the convenience of the reader.

A. Detached Eddy Simulation

The Detached Eddy Simulation (DES) is a hybrid scheme in which an existing single RANS turbulence model, typically the Spalart-Allmaras or Menter $k-\omega$ SST models, is utilized in both its RANS sense and as a subgrid model. The RANS model is used in its original sense close to the wall, within turbulent attached boundary layers, while in separated regions where the grid spacing is smaller than the turbulent zone or layer, the model acts as a filter similar to classic LES subgrid scale (sgs) filters. The distance from the wall, d, in classic RANS models is replaced by a modified distance from the wall, $\overline{d}$, which is defined as

$$\overline{d} = min(d, c_{DES}\Delta) \tag{6}$$

where Δ is the length of the largest side of the cell ($max(\Delta x, \Delta y, \Delta z)$) and c_{DES} is an empirical constant, usually taken to be 0.65.

The sgs model based on the use of $\overline{d}$ is simplistic, but the results using the DES is directly coupled to the grid size. Thus, care must be taken in grid generation as large aspect ratio cells in any direction will impact the efficacy of the solution. As many RANS grids routinely apply large aspect ratio cells (typically in the span direction along a wing), these existing grids may not provide dramatically improved results with DES.

B. GT–HRLES

Another blended hybrid RANS/LES approach,[20,22] denoted as the GT–HRLES method, combines the two-equation $k-\omega$ RANS model with a one-equation sub-grid turbulence kinetic-energy model (i.e., k-equation). This approach has been successfully applied to dynamically pitching airfoil simulations[22,23] and for wind-turbine blade simulations,[24] and it has recently been initially extended[25] for application with unstructured grid methodologies.

The closure information exchange for this model occurs via the turbulent kinetic energy, k. In this work, the RANS turbulence model applied is the Menter $k-\omega$ SST turbulence model,[26] based on its success in similar CFD applications of interest.[27–29]

The Menter $k-\omega$ SST turbulence model solves two differential equations that describe the turbulent kinetic energy, as well as an approximation for the length scale based on the dissipation per unit turbulent kinetic energy, ω. These equations are given by:

$$\frac{\partial}{\partial t}(\rho k) + \frac{\partial}{\partial x_j}(\rho u_j k) = \tau_{ij}^{rans}\frac{\partial u_i}{\partial x_j} - \beta^*\rho\omega k + \frac{\partial}{\partial x_j}\left[(\mu + \sigma_k\mu_T)\frac{\partial k}{\partial x_j}\right] \tag{7}$$

$$\frac{\partial}{\partial t}(\rho\omega) + \frac{\partial}{\partial x_j}(\rho u_j \omega) = \frac{\gamma\rho}{\mu_T}\tau_{ij}^{rans}\frac{\partial u_i}{\partial x_j} - \beta\rho\omega^2 + \frac{\partial}{\partial x_j}\left[(\mu + \sigma_\omega\mu_T)\frac{\partial \omega}{\partial x_j}\right] + 2(1-F_2)\rho\sigma_{\omega 2}\frac{1}{\omega}\frac{\partial k}{\partial x_j}\frac{\partial \omega}{\partial x_j} \tag{8}$$

where the *rans* superscript is used to denote the use of the Reynolds-averaged Reynolds-stress tensor. Menter[26] indicates that the production terms ($\tau_{ij}^{rans}\frac{\partial u_i}{\partial x_j}$) can be modeled directly with $\mu_T\Omega^2$ where Ω is the vorticity magnitude defined by $\Omega^2 = (\partial w/\partial y - \partial v/\partial z)^2 + (\partial u/\partial z - \partial w/\partial x)^2 + (\partial v/\partial x - \partial u/\partial y)^2$.

An equation for the subgrid turbulent kinetic energy (k^{sgs}) can be expressed as

$$\frac{\partial}{\partial t}(\overline{\rho}k^{sgs}) + \frac{\partial}{\partial x_j}(\overline{\rho}\widetilde{u_j}k^{sgs}) = \tau_{ij}^{sgs}\frac{\partial \widetilde{u_i}}{\partial x_j} - C_\epsilon\frac{(k^{sgs})^{3/2}}{\Delta} + \frac{\partial}{\partial x_j}\left[\left(\frac{\widetilde{\mu}}{Pr} + \frac{\mu_{sgs}}{Pr_t}\right)\frac{\partial k^{sgs}}{\partial x_j}\right] \tag{9}$$

where C_ϵ and C_ν are model coefficients governing the dissipation and production of k^{sgs}, respectively. This evolution equation has been successfully utilized by Kim and Menon.[30] It is worth emphasizing that the RANS k-equation solves for the *total* kinetic energy while the LES k^{sgs} is only modeling that not fully resolved on the computational mesh.

The RANS equations of motion and kinetic energy equation are linearly merged to form the hybrid model based on the recommendations of Baurle *et al.*[19] and Speziale:[31]

$$\frac{\partial}{\partial t}(\vec{F}) + \frac{\partial}{\partial x_j}(\widetilde{u_j}\vec{F}) = \frac{\partial}{\partial x_j}(\vec{G}^{trans}) + \vec{G}^{src} + \frac{\partial}{\partial x_j}(\vec{G}^{hybrid}_{T_{trans}}) + \vec{G}^{hybrid}_{T_{src}} \tag{10}$$

where $\vec{E} = \{\rho, \rho\widetilde{u_j}, \rho E, \rho k\}$ and the right hand side of the equation consists of the original transport ($\vec{G}^{trans}$) and source ($\vec{G}^{src}$) vectors excluding the fluctuating turbulence terms, which have been formulated into new vectors, $\vec{G}_{T_{trans}}$ and $\vec{G}_{T_{src}}$ that will be hybridized. The hybridization of the two $\vec{G}_T$ terms occurs via a simple linear formulation $\vec{G}^{hybrid}_T = F\vec{G}^{rans}_T + (1-F)\vec{G}^{sgs}_T$. The function F which is used as the switch mechanism is $F = tanh(x^4)$ where $x = max(\frac{2\sqrt{k}}{0.09\omega y}, \frac{500\nu}{y^2\omega})$.

In this implementation of GT–HRLES, realizability constraints to maintain physical values of the turbulent kinetic energy are not strictly enforced. Further details of the development of this hybridization technique can be found in Sanchez-Rocha and Menon.[22] It should be noted that Sanchez-Rocha[20] has recently published a new version of this model that includes new terms that preserve the consistency of the hybrid equations, and proposes a localized dynamic approach to compute all the model coefficients locally in space and time.

III. Correlation Experiment Description

The numerical results are compared with experiments conducted with a flatback version of the DU97-W-300 airfoil. The airfoil investigated is a flatback version of the Delft University DU97-W-300 airfoil.[32] The flatback airfoil was created from the original airfoil by adding thickness about the mean camber line over the aft portion of the airfoil, leaving a blunt trailing edge with a thickness of 10% of the chord (see Fig. 1). This airfoil, along with the original DU97-W-300 airfoil, was tested in the Virginia Tech Stability Wind Tunnel and both aerodynamic and aeroacoustic measurements were made.[6,18] Measurements were also made with a splitter plate with length equal to the flatback base height attached to the center of the base. The airfoil models had a chord of 0.9144 meters and a span of 1.8 meters, allowing measurements at chord Reynolds numbers up to 3.2×10^6. Measurements were made of the airfoil model profiles, and smoothed versions of the measured flatback profile were used to define the geometry for the numerical simulations. Detailed descriptions of the instrumentation and test setup are available,[18,33] along with some preliminary results. Included in the data were microphone measurements of the trailing edge vortex-shedding noise for an observer located in the symmetry plane of the airfoil model, at a distance 3.12 meters from the trailing edge and at an angle of 112 degrees from the streamwise (x) axis.

IV. Computational Methodologies

A. SACCARA

SACCARA[34] is a multi-block, structured grid finite- volume code that solves the steady or unsteady compressible Navier-Stokes equations. The nominal flux scheme is the second order Symmetric Total-Variation-Diminishing (STVD) scheme.[35] The STVD scheme is generally too dissipative for unsteady simulation of turbulent flows, thus the code has been modified to incorporate a low-dissipation version of the STVD

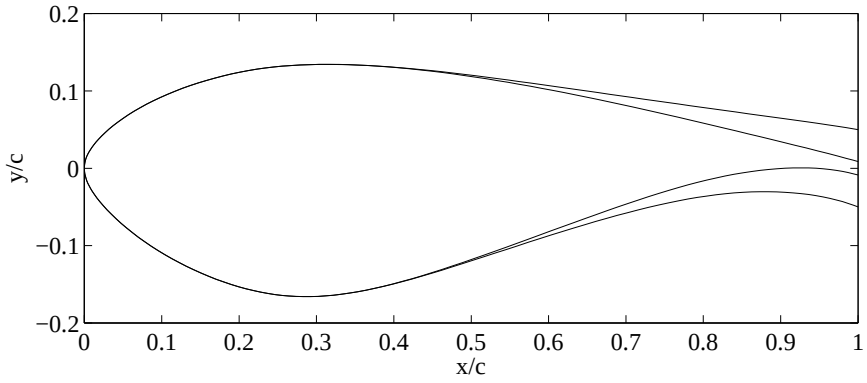

Figure 1. DU97-W-300 and DU97-flatback airfoils.

scheme. This low-dissipation scheme employs a wavelet-based flow sensor[36] to reduce or eliminate numerical dissipation in regions of smooth flow. Time-accurate computations are performed using a 2^{nd}-order implicit backward difference scheme. Hybrid RANS/LES models available in SACCARA include the Detached Eddy Simulation (DES)[37] model and the Partially-Averaged Navier-Stokes (PANS) model.[38]

B. OVERFLOW

OVERFLOW[39] uses overset, structured grids to solve the flow around complex and moving geometries. This code was chosen since it has been successfully applied to numerous complex, moving body environments such as rotorcraft[40–42] and to wind turbines.[43,44]

OVERFLOW solves the compressible form of the unsteady RANS equations using an implicit, finite-difference approach with overset grids. The method is 1^{st}- or 2^{nd}-order accurate in time with 4^{th}-order central differences for spatial derivatives. The method uses 2^{nd}- and 4^{th}-order central difference dissipation terms for stability. The use of overset grids to simulate complicated configurations and moving frames of reference has been in practice for many years and can be considered well-established. Overset grids dramatically reduce the difficulties associated with structured mesh generation for complicated configurations. OVERFLOW employs low Mach number preconditioning to handle numerical difficulties associated with low-speed simulations. A recent advancement for *unsteady* low Mach preconditioning (ULMP) has been published by.[45] This method can significantly improved convergence rates for low-speed flows.

The DES model[37] based on either the Spalart-Allmaras one-equation or Menter $k-\omega$ SST turbulence model is available, and GT–HRLES has been implemented into this version of OVERFLOW.[28]

C. FUN3D

FUN3D implicitly solves the Reynolds Averaged Navier-Stokes (RANS) equations using node-centered unstructured mixed topological meshes[46,47] and has been successfully utilized for a number of applications that encompass the aerospace spectrum.[48,49] FUN3D can resolve the RANS equations for both compressible and incompressible[50] flows. Steady state solutions are obtained using a 1^{st}-order backward Euler scheme with local time stepping, while time accurate solutions utilize the 2^{nd}-order backward differentiation formula (BDF). The resulting linear system of equations is solved using a point-implicit relaxation scheme. The Roe flux difference splitting technique[51] is utilized to calculate the inviscid fluxes on the control volume faces, while viscous fluxes are computed using a finite volume formulation that results in an equivalent central difference approximation.

The DES model[37] based on the Spalart-Allmaras one-equation turbulence model is available within FUN3D and the GT–HRLES method has been extended for unstructured topologies and implemented into FUN3D.[25]

V. Computational Setup

A series of 2-D and 3-D simulations have been conducted on the DU97W300 flatback airfoil at an angle-of-attack (α) of 4° and 10°. These simulations are repeated with a splitter-plate attached at the trailing edge. The splitter-plate is intended to alter the vortex shedding properties.

A. SACCARA

For the computations discussed in this work, SACCARA solutions were computed using the original DES hybrid model, based on the one-equation Spalart-Allmaras turbulence model. The STVD scheme was used upstream of the trailing edge, while the wake region was computed using the low-dissipation scheme. Initially, a steady, two-dimensional RANS solution was found using the STVD scheme in the entire domain. The unsteady simulation was then initiated, using the low-dissipation scheme downstream of the trailing edge. The initial transient induced by the change in numerical schemes was sufficient to trigger vortex-shedding in the wake.

The SACCARA simulations were run on a series of grids with varying spanwise domain width Z and number of spanwise grid cells N_z. Each two-dimensional spanwise section of the grid was a C-grid containing 400 cells along the airfoil surface, 188 grid cells normal to the upper and lower surfaces, 120 cells across the airfoil base, and 300 cells in the streamwise direction downstream of the trailing edge. This resulted in 2.24×10^5 total grid cells in each two-dimensional section. The wall-normal grid spacing at the upper and lower surfaces was $\Delta/c < 2.9 \times 10^{-6}$, resulting in a y^+ value for the first grid cell off the wall of less than 0.4 for the RANS solutions. The outer boundary of the domain extended to at least $50c$ in all directions. Spanwise periodic boundary conditions were applied for all simulations. The trailing edge region of the grid is pictured in Figure 2.

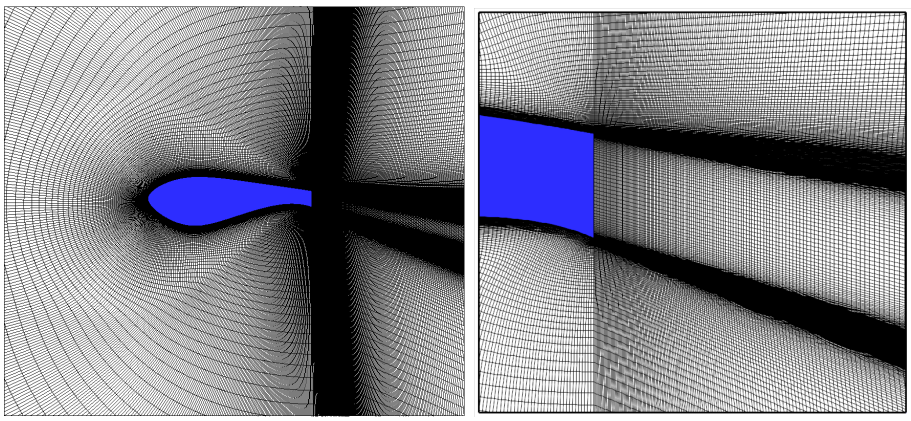

Figure 2. Grid used for SACCARA simulations, with trailing edge detail.

Both steady RANS and unsteady DES simulations were run with SACCARA at a Reynolds number of $Re_c = 3 \times 10^6$ and a Mach number of 0.17. The time step used for all unsteady SACCARA results was $\Delta t U_\infty/c = 5 \times 10^{-4}$. This resulted in the dominant sinusoidal vortex shedding period being resolved by approximately 1000 time steps. For each physical time steps a total of 15 subiteration steps were taken.

Boundary layer transition was specified at $x/c = 0.05$ on the upper surface and $x/c = 0.10$ on the lower surface for all simulations. In SACCARA this was accomplished by explicitly setting the eddy viscosity to zero upstream of the transition locations.

B. OVERFLOW

All simulations are conducted with a free-stream Mach number (M) of 0.2 and a Reynolds number (Re) of approximately 3 million. All simulations are assumed to be fully turbulent with fixed transition points

located at 0.05 and 0.1 x/c from the leading edge on the suction and pressure sides respectively.

Along the airfoil surface, a no-slip, rigid, adiabatic wall condition is enforced. A free-stream characteristic boundary condition is imposed at the far-field boundary located $50c$ from the surface in the normal and streamwise directions. A spanwise periodic boundary condition is imposed for all 3-D simulations. The spacing in the periodic direction is uniform with a spanwise extent of $1c$ using sixty-five equally-spaced spanwise locations ($c/65$) for all 3-D simulations.

A body-fitted, O-type, finite-difference mesh is used to define the airfoil surface, as illustrated in Fig. 3b). The wall-normal spacing near the trailing edge is held to less than $10^{-6}c$ with a hyperbolic stretching function extending the grid outward in the normal direction. The *near-body* (NB) airfoil mesh has an outer boundary of approximately $1c$ with a maximum normal spacing of $0.025c$ and maximum stretching of approximately 9% using 141 points. Clustering in the streamwise direction occurs at the leading-edge stagnation point and in the vicinity of the sharp corners at the trailing-edge (Fig. 4a) and splitter-plate (Fig. 4b). The finest spacing in the streamwise direction is $10^{-4}c$ and the maximum stretching is limited to 5% requiring 989 points in total. Smoothing is applied to avoid poor resolution near the sharp convex and concave corners of the flat-back and splitter-plate grids. The effect of the concave corner in the splitter-plate mesh is easily visualized by the fine clustering of points eminating at approximately 45°. The thinness of the splitter-plate base area resulting in some difficulty with the wake resolution. Future grid-refinement studies are needed to address this affect.

A series of hierarchal, Cartesian, overset meshes are employed to extend the domain to the user-specified far-field location (Fig. 3a). The finest Cartesian mesh (Level-1) has a resolution of $0.025c$ in the stream-wise and normal directions to match the NB resolution. Grid resolutions double with each subsequent overset level. The NB mesh is fully immersed within Level-1 with second-order accurate (*double-fringe*) overset method. Telescoping, hierarchal meshes of this style are critical for efficiently maintaining the necessary resolution for wake studies with structured grids. Each 2-D plane consists of 139,449 grid points.

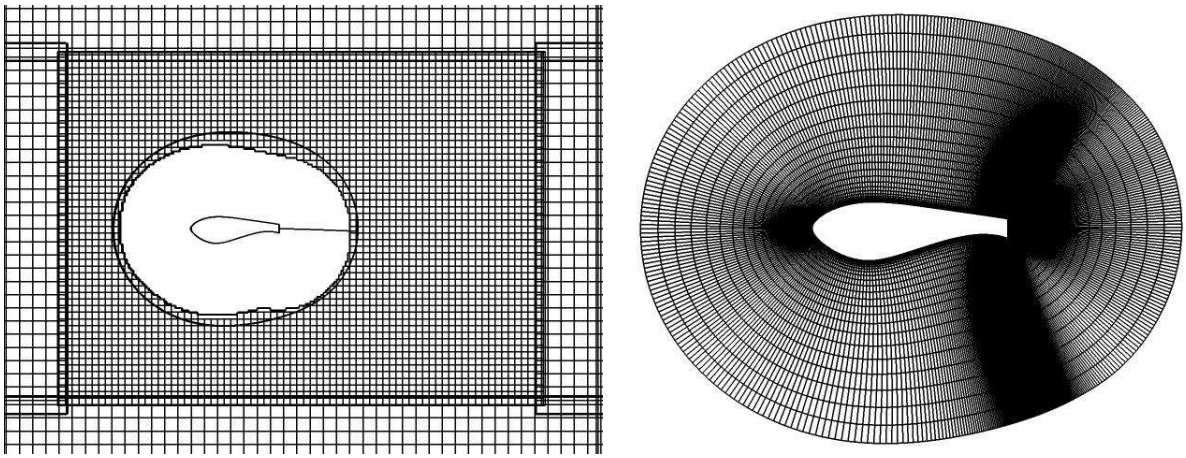

(a) Telescoping overset meshes

(b) Near-body mesh O-mesh

Figure 3. OVERFLOW overset meshes.

2-D simulations were conducted using the steady-state Spalart-Allamaras (SA) and two-equation $k-\omega$ SST[26] (SST) steady-state RANS models. These two models are widely used in industry for aerodynamic predictions and are included for comparison. Steady-state RANS simulations are assumed converged when the integrated aerodynamic lift coefficients (C_L) has reached a steady value. As there is no *converged* solution for unsteady simulations, the time-averaged coefficients are reported instead. Two-dimensional GT–HRLES simulations were also run for both geometries and both α's. However, only GT–HRLES simulations were conducted in 3-D.

All unsteady simulations, except where noted, use a constant time-step of $\Delta t = 0.001$. Based on a

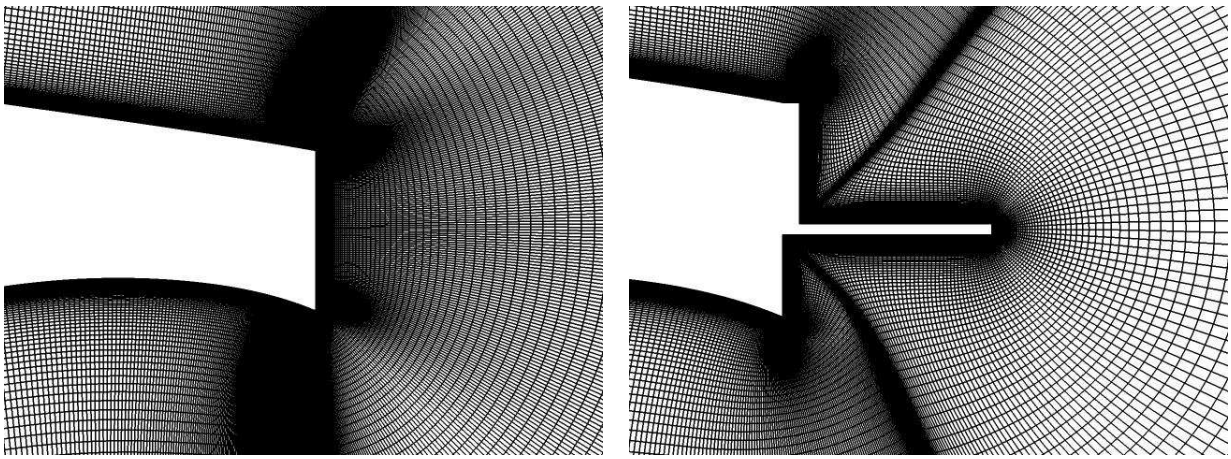

(a) Flatback trailing edge (b) Splitter-plate trailing edge

Figure 4. Trailing-edge OVERFLOW meshes.

presumed vortex shedding (reduced) frequency of $St = 0.2$, this yields approximately 500 timesteps per cycle. For added stability and convergence rates, the time-step size for the 10° splitter-plate simulations was reduced to 0.0005. Newton sub-iterations were performed at every time-step to achieve higher temporal accuracy (approximately 2^{nd}-order). The number of iterations was manually set to achieve 3 orders-of-magnitude drop in the L_2-norm of the right-hand-side residual. The required number ranged from 8 sub-iterations for the 4° cases up to 16 for the 10° 3-D splitter-plate GT–HRLES case.

C. FUN3D

For the FUN3D unstructured simulations, a free-stream Mach number (M) of 0.2 and a Reynolds number (Re) of 3 million were applied to the flatback airfoil at 4° and 10° angles of attack. All simulations are assumed to be fully turbulent, using the GT–HRLES and Mentor $k-\omega$ SST models, and were run with the compressible version of the methodology. The simulations are 2^{nd}-order in space and time and were resolved using a Roe scheme without flux limiters. The time step, Δt, was set to 0.005, which is the same time step applied for the OVERFLOW simulations, but with a different non-dimensionalization applied. This provides approximately 500 time steps per shedding cycle.

A body-fitted, mixed element mesh (Fig. 5) is used to define the control volume for the simulations. The 2-D mesh is comprised of 176,468 nodes on 2 identical planes for a total node size of 352,936. Of this 93,616 hex cells comprised the boundary layer region about the airfoil, and 160523 prismatic cells formed the inviscid region. The wall normal spacing near the trailing edge is approximately $8.5c \times 10^{-6}$. The outer boundary of the mesh is rectangular with the freestream boundaries located $20c$ upstream and $30c$ downstream of the airfoil surface. The upper and lower freestream boundaries are each $20c$ from the surface. The structured OVERFLOW surface mesh was used as the geometry definition for the unstructured mesh. Tangential grid spacing along the wall was identical to the OVERFLOW mesh.

VI. Results

The results of the numerical simulations are reported in this section, including aerodynamic and aeroacoustic quantities. For comparison with the numerical results that are presented in the following sections, a limited portion of the aerodynamic and aeroacoustic data from the Virginia Tech stability wind tunnel for the DU97-flatback are given in Table 1 for $Re_c = 3 \times 10^6$, along with estimated experimental uncertainties.

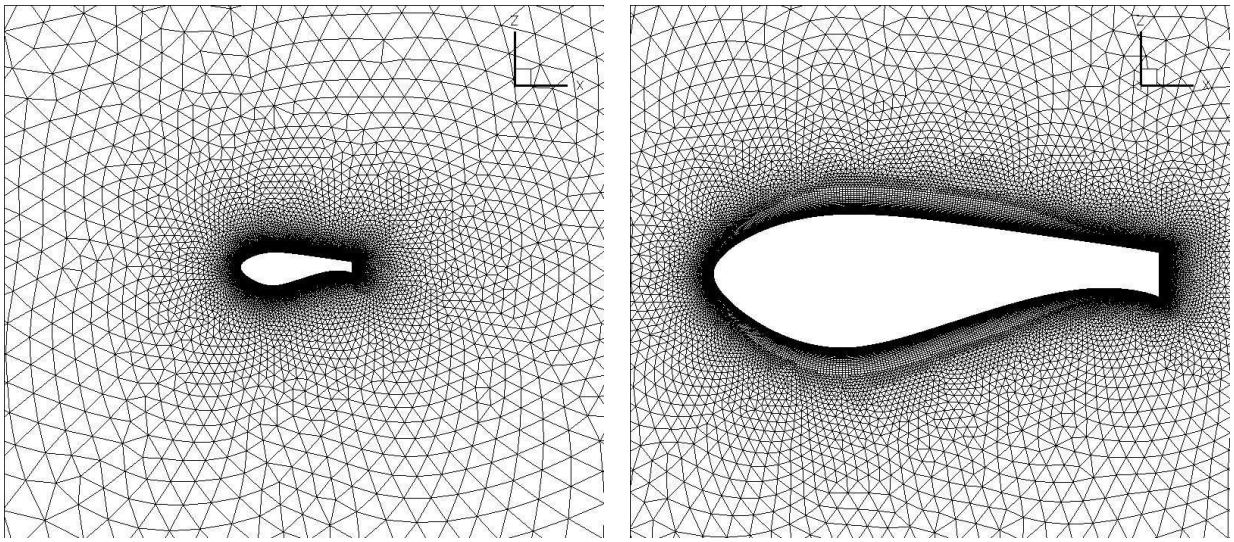

(a) (b)

Figure 5. Unstructured flatback airfoil mesh utilized for FUN3D simulations.

There are several important considerations to bear in mind when interpreting the data and its relation to the numerical simulations. The measured lift coefficient is reported with trip strips at $x/c = 0.1$ on the lower surface and $x/c = 0.05$ on the upper surface, consistent with the tripping used in the numerical simulations. However, drag coefficient and the peak vortex-shedding noise for $\alpha = 4^\circ$ were measured only for the clean (un-tripped) configuration. Noise was measured for an effective angle of attack of both $\alpha = 4^\circ$ and $\alpha = 11^\circ$; the latter α was slightly different from the computational setup of $\alpha = 10^\circ$, but the difference is not expected to be significant relative to the uncertainty of both the experiment and the computational models. The measured peak SPL for the clean $\alpha = 11^\circ$ case was 89.5 dB, or 4 dB lower than for the tripped case. This suggests that the SPL for the $\alpha = 4^\circ$ tripped case may also be higher than the 94 dB value for the clean case. Note also that the experimental lift coefficients were obtained by integrating the measured surface pressures and do not include the loading from the splitter plate surface, which was not instrumented.

Table 1. DU97-flatback experimental data for $Re_c = 3 \times 10^6$. Quantities measured with boundary layer tripping unless denoted with superscript * which indicates quantity was measured only for the clean (un-tripped) configuration.

Splitter Plate	α, deg.	C_L	C_D	St	SPL, dB
No	4	0.81 ± 0.09	$0.060^* \pm 0.005$	0.24 ± 0.01	$94.0^* \pm 1$
Yes	4	0.71 ± 0.09	$0.032^* \pm 0.005$	0.30 ± 0.01	79.0 ± 1
No	11	1.57 ± 0.13	$0.055^* \pm 0.005$	0.24 ± 0.01	93.5 ± 1
Yes	11	1.52 ± 0.13	$0.030^* \pm 0.005$	0.27 ± 0.01	76.9 ± 1

A. Aerodynamic Performance

The integrated aerodynamic lift and drag coefficients for the 2-D and 3-D flatback airfoil simulations have been assembled in Table 2. The time-averaged C_L and C_D are given for unsteady simulations and the converged solution for steady-state. The intensity of fluctuations in the unsteady coefficients are measured

Table 2. Integrated aerodynamic loading simulations for the DU97W300 flatback airfoil. Results are steady-state or time-averaged lift/drag coefficient (C_L) and RMS value ($C_L^{\prime rms}$). For time-accurate simulations, the lift oscillation reduced frequency (Strouhal Number) is given. 3-D Grid information is given as spanwise depth/number of points. All HRLES runs are assumed to be unsteady, while all RANS runs are assumed to be steady unless otherwise noted.

α	Grid	Turbulence Method	Code Used	C_L	C_D	$C_L^{\prime rms}$	$C_D^{\prime rms}$	Strouhal Number
4	2D	SA	OF	0.88	0.037	–	–	–
4	2D	SST	OF	0.858	0.034	–	–	–
4	2D	SST	FUN3D	0.874	0.039	–	–	–
4	2D	SST (Unsteady)	FUN3D	0.908	0.055	0.0491	0.0053	0.210
4	2D	SA	SAC	0.88	0.042	–	–	–
4	2D	SADES	SAC	0.85	0.135	0.14	0.015	0.21
4	2D	GT–HRLES	OF	0.883	0.144	0.107	0.024	0.230
4	2D	GT–HRLES	FUN3D	0.906	0.052	0.0413	0.0042	0.206
4	0.5c/33	GT–HRLES	OF	0.844	0.056	0.027	0.007	0.195
4	$0.2c/64$	SADES	SAC	0.87	0.10	0.11	0.015	0.20
4	$0.4c/64$	SADES	SAC	0.86	0.11	0.11	0.014	0.20
4	$0.8c/64$	SADES	SAC	0.89	0.084	0.05	0.0098	0.19
10	2D	SA	OF	1.62	0.042	–	–	–
10	2D	SST	OF	1.59	0.046	–	–	–
10	2D	SST	FUN3D	1.618	0.046	–	–	–
10	2D	SST (Unsteady)	FUN3D	1.638	0.052	0.0232	0.0052	0.198
10	2D	SADES(Steady)	SAC	1.63	0.047	–	–	–
10	2D	SADES	SAC	1.58	0.133	0.13	0.023	0.20
10	2D	GT–HRLES	OF	1.630	0.103	0.076	0.018	0.213
10	2D	GT–HRLES	FUN3D	1.658	0.054	0.0319	0.0071	0.195
10	0.5c/33	GT–HRLES	OF	1.56	0.078	0.078	0.017	0.183
10	$0.4c/64$	SADES	SAC	1.63	0.096	0.08	0.019	0.19

through the root-mean-squared (RMS) and are also shown in Table 2. Additionally, the effective Strouhal number that indicated the reduced frequency of the fluctuating lift is reported. This frequency has been normalized by the flatback base height, h, to allow comparisons with other bluff-body flow solutions (see below).

For the flatback airfoil, it is readily observed that the mean lift coefficient remains within 5.5% no matter what the grid, code or turbulence method utilized. The numerical predictions also fall within the experimental range of lift coefficient, albeit very close to the upper experiment bound. The mean drag coefficient, however, does show significant variation with all of these parameters. The 2-D steady drag predictions using RANS are $1/3 - 1/2$ lower than the experimental data, interestingly these are in the opposite direction to the expected trends as the experiment was untripped. This appears to be an artifice of running the simulation in the steady-mode as the URANS drag predicted by $k-\omega$ SST using FUN3D is within the experimental bounds, although it too is slightly lower than the experimental mean. The 2D HRLES predictions by SACCARA and OVERFLOW are within about 6% of each other, but over predict the drag by over 100%. The FUN3D 2-D HRLES prediction falls within the experimental bounds. The OVERFLOW and SACCARA 3-D results confirm prior results[52] that grid studies for infinite wing (airfoil) simulations for LES and hybrid RANS/LES are critical to achieve accurate drag computations. Two-dimensional hybrid

Table 3. Comparison of 2-D and 3-D Fluctuations for the Flatback Airfoil using SACCARA

α (°)	Grid	Mode	$\overline{C_L}$	$\overline{C_D}$	$C_L'^{rms}$	$C_l'^{rms}$	$C_D'^{rms}$	$C_d'^{rms}$	St
4	2D	Steady	0.88	0.042	–	–	–	–	–
4	2D	Unsteady	0.85	0.135	0.14	0.14	0.015	0.015	0.21
4	$2c/64$	Unsteady	0.87	0.10	0.11	0.10	0.015	0.024	0.20
4	$4c/64$	Unsteady	0.86	0.11	0.11	0.11	0.014	0.025	0.20
4	$8c/64$	Unsteady	0.89	0.084	0.05	0.05	0.0098	0.014	0.19
4	$8c/128$	Unsteady							
10	2D	Steady	1.63	0.047	–	–	–	–	–
10	2D	Unsteady	1.58	0.133	0.13	0.13	0.023	0.023	0.20
10	$4c/64$	Unsteady	1.63	0.096	0.08	0.08	0.019	0.024	0.19

RANS/LES predictions of the drag have been previously shown within structured meshes to be high,[25,28,52] but it is unclear given these limited studies if grid independence (and hence accurate drag predictions) has been reached. The fact that the SACCARA and OVERFLOW codes exhibit large variations in the low angle of attack data, while FUN3D does not implies that differences in implementation (boundary condition, mesh, numerical scheme, steady/unsteady) may be the source of the differences. The 3-D GT-HRLES result for OVERFLOW falls within the experimental range, while the SADES results from SACCARA still remain higher than the experimental bounds. Flow-field visualizations included later in the paper shed some light on possible reasons for differences in drag coefficient predictions for the 3D simulations.

These observations can be extended to the fluctuating values of the respective coefficients. For the 3-D simulations, the Strouhal number is within 5% no matter what method is applied, however the value of approximately 0.20 is 13% below the experimental bounds of the experimental Strouhal number. The one exception to this is the 2-D prediction using GT–HRLES within OVERFLOW, which predicts a value of 0.23, which is the lower experimental bound. However, since once again, it is noted that the 2-D hybrid simulations using OVERFLOW and SACCARA generate values that are $5-20\%$ higher than their 3-D counterparts, the 3-D correlation is not as accurate.

A comparison of the sectional and full-span fluctuating lift and drag coefficients was done using the SACCARA code predictions. At any instant in time the integrated forces at each 2-D section are oscillating. If all of the 2-D sections are in perfect phase, then the 2-D and 3-D force fluctuations will be equal. If they are not in phase, there is a cancellation effect when the force of all the 2-D sections are combined to compute the 3-D force. It is readily observed in Table 3 that the lift is almost perfectly in phase along the span for these simulations, as the sectional lift fluctuation, C_l', is equal (to 2 digits) to the 3-D lift fluctuation, C_L'. The drag fluctuations indicate however that drag is not in phase. The sectional drag fluctuation values, C_d', are higher by 40-80% than the 3-D drag fluctuations, C_D', in all evaluations. Thus, while a 2-D simulation may be utilized to determine unsteady lift characteristics, a full 3-D simulation is necessary for drag fluctuation analysis.

Relative to similarly shaped sharp trailing edge airfoils, the flat-back geometry is expected to incur an increased C_D due to the large base pressure. The addition of the splitter-plate is expected to reduce the significance is this by limiting highly coherent vortex shedding. Results for the geometry with the addition of the splitter plate is provided in Table 4. These runs were accomplished using the OVERFLOW code only. When these tabulated values are compared with the results in Table 2, it is clear that overall lift coefficient is decreased, as is the drag coefficient when compared to the original flatback configuration, as predicted by the experiment. The 2-D RANS results for lift fall within the experimental bounds, while the 2-D GT-HRLES result is slightly above the bound. In this instance, the numerically predicted drag coefficient is higher than the experimental values, which is the expected result as the experimental values were obtained using an untripped configuration. When comparing the performance parameter L/D, the

Table 4. Integrated aerodynamic loading simulations for the DU97W300 flatback airfoil with splitter plate. Results are steady-state or time-averaged lift/drag coefficient (C_L) and RMS value ($C_L^{\prime rms}$). For time-accurate simulations, the lift oscillation reduced frequency (Strouhal Number) is given. 3-D Grid information is given as spanwise depth/number of points.

α	Grid	Turbulence Method	Code Used	C_L	C_D	$C_L^{\prime rms}$	$C_D^{\prime rms}$	Strouhal Number
4	2D	SA	OF	0.79	0.044	-	-	-
4	2D	SST	OF	0.80	0.043	-	-	-
4	2D	GT–HRLES	OF	0.844	0.037	0.019	0.002	0.220
4	0.5c/33	GT–HRLES	OF	0.74	0.041	0.026	0.0032	0.282
10	2D	SA	OF	1.50	0.043	-	-	-
10	2D	SST	OF	1.53	0.059	-	-	-
10	2D	GT–HRLES	OF	1.61	0.043	0.020	0.005	0.212
10	0.5c/33	GT–HRLES	OF	1.34	0.064	0.048	0.010	0.170

splitter plate provides typically a $15-20\%$ increase in L/D. The numerically predicted values for the L/D were approximately 18-22, which fall within the L/D experimentally-bounded values for the 4° case, but the numerically predicted L/D values at 10° fall below the lower experimental bound.

The aerodynamic effect of the splitter-plate can be visualized in the pressure coefficient (C_p) in Fig. 6 for the 3-D OVERFLOW simulations (GT–HRLES) at $\alpha = 4^\circ$ with and without the splitter-plate. The x-axis has been normalized by c, the chord length not including the splitter-plate's length. The results are derived using the time- and span-averaged surface pressure. As the airfoils have the same basic geometry, there is little difference seen near the leading-edge. However, the upstream effects of the trailing-edge splitter-plate are quickly felt on both the suction and pressure sides. The peak-suction ($x/c = 0.2$) and peak-pressure ($x/c = 0.26$) are reduced by 5 and 10%, respectively. There is an anomaly on the pressure side at $x/c = 0.3$ which corresponds to the maximum camber location. This anomalous pressure discontinuity is being further investigated. There is little apparent affect from the splitter-plate further downstream on the pressure side. The suction reduction by the splitter-plate continues along the extent of the suction side and is most pronounced at the trailing edge. As was seen in the integrated lift and drag results above, both are predicted lowered with the addition of the splitter-plate.

Time-averaged streamwise ($\overline{U}$) and transverse ($\overline{V}$) velocities and their correlation ($\overline{u'v'}$) are shown along the mid-span location in Figs 7(a-f). Comparing $\overline{U}$ reveals significant differences in the trailing-edge recirculation region as well as the location of the separation bubble along the airfoil suction side. The latter is further aft with the addition of the splitter-plate. Additionally, the recirculation zone is extended downstream further. Based upon the mean C_D results in Tables 2 and 4 shows a lowering of the drag with the inclusion of the plate. The splitter-plate appears to act as a flow straightener lessening the intensity of the recirculation zone. This effect can also been seen in the plot of the $\overline{u'v'}$ correlation (Figs 7c,f)). There, location of significant $\overline{u'v'}$ is moved from just after of the body to well downstream with the addition of the splitter-plate; likewise, the intensity is also attenuated.

B. Spectral Analysis of Lift Coefficient Fluctuation

A spectral analysis has been applied to the time-dependent lift coefficient $C_L(t)$ signal for both 4° and 10° OVERFLOW cases. The results are shown in Fig. 8. There, both 2- and 3-D simulations using HRLES are shown for each α. The frequency of the fluctuations are normalized by the flatback base height (h) instead of the chord (c) for direct comparison with bluff-body Strouhal number (St) correlations. From the 2-D simulations, it is clear that the primary mode is at $St = 0.21$ which fits well with reported bluff-body vortex shedding frequencies for turbulent flows, but deviates somewhat from the reported experimental value. The

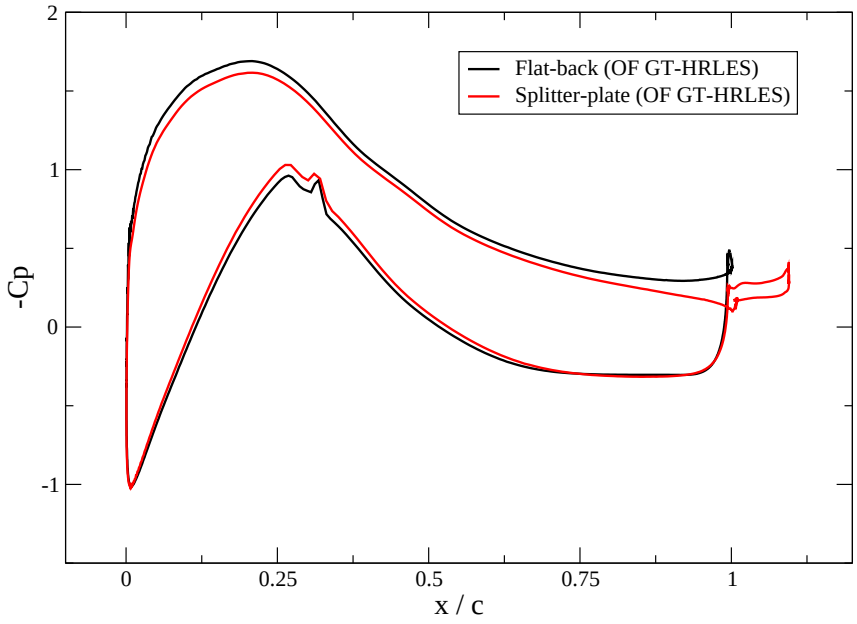

Figure 6. c_p **plot for flat-back and splitter-plate 3-D simulations at** $\alpha = 4^\circ$ **using OVERFLOW GT–HRLES.**

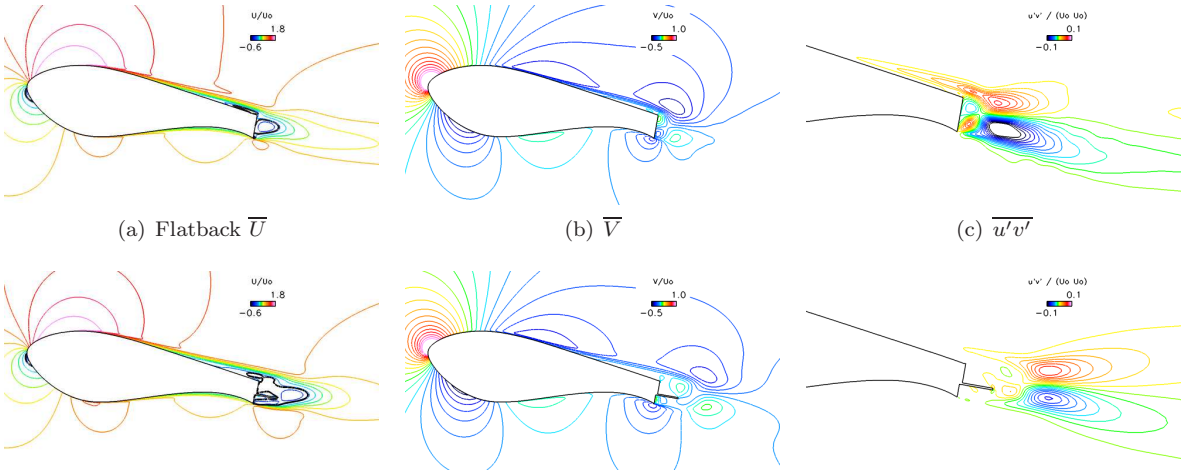

(a) Flatback $\overline{U}$ (b) $\overline{V}$ (c) $\overline{u'v'}$

(d) Splitter-plate $\overline{U}$ (e) $\overline{V}$ (f) $\overline{u'v'}$

Figure 7. Streamwise and spanwise time-averaged mean velocity for $\alpha = 10^\circ$ **computed at the mid-span location of the 3-D simulations using OVERFLOW with GT–HRLES.**

presence of 3-D flow features leads to a less tonal signal when comparing the 2-D and 3-D simulations. The shedding frequency for the flatback simulations are both reduced to $St = 0.195$ and 0.183 for the 4° and 10° cases, respectively. The splitter-plate simulations resulted in significant changes depending on α. For $\alpha = 4°$, the shedding frequency is significantly increased to $St = 0.282$ while it is largely unaffected in the 10° case. The amplitude of C'_L is attenuated with the addition of the splitter-plate for $\alpha = 4°$ yet again is unaffected for $\alpha = 10°$.

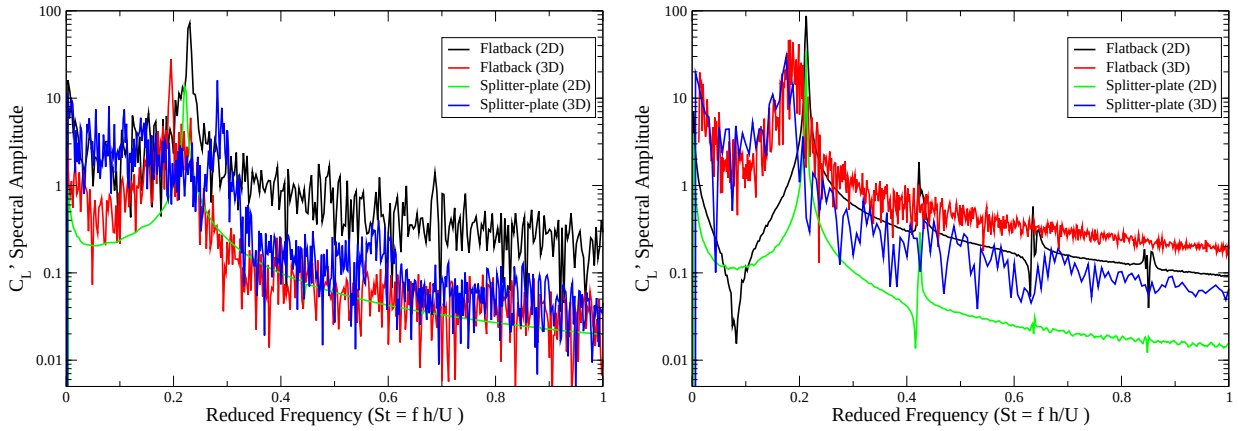

(a) $\alpha = 4°$ (b) $\alpha = 10°$

Figure 8. Spectral analysis of fluctuation lift coefficient (C'_L) for unsteady LES simulations. Spectral amplitude versus reduced frequency ($St = fh/U_\infty$).

C. Estimate of Vortex-Shedding Noise

Airfoils with a blunt base (trailing edge), such as the flatback airfoil, produce tonal noise associated with the interaction of vortex shedding in the airfoil wake with the trailing edge. This noise source can be modeled as a low-frequency dipole, with far-field sound intensity proportional to the mean-square of the lift fluctuation produced by the shedding. This type of model has been applied successfully to prediction of vortex-shedding noise from circular cylinders.[53] In addition to the assumption of low Mach number, the primary assumptions are that the acoustic wavelength λ is larger than the characteristic dimension of the scattering body, in this case the airfoil chord c, and that the distance from sound source to observer, R, is much larger than λ. Consider the case of a wing section with invariant two-dimensional shape and spanwise width Z, and assume that the vortex-sound source is perfectly correlated along the span. For an observer in the plane of the center section, at an angle θ with the x-axis, the vortex sound intensity relation is

$$I = \frac{\overline{p'^2}}{\rho a} = \frac{\sin^2\theta}{32a^3R^2}\rho U_\infty^6 Z^2 C'^2_{L^{rms}}(St)^2. \tag{11}$$

The sound intensity is thus related to the density and speed of sound of the surrounding fluid, the free stream velocity, observer position, the mean-square of the lift coefficient fluctuation and the Strouhal number associated with the vortex shedding.

Now consider the case of imperfectly correlated sources of sound along the spanwise direction. This can occur for the flatback airfoil if three-dimensional vortex-shedding modes are present and alter the phase of the sectional lift coefficient signal along the span. The correlation function of the lift coefficient fluctuation

is defined as

$$R_{LL}(\xi) \equiv \frac{\overline{C_l'(z,t)C_l'(z+\xi,t)}}{\overline{C_l'^2}}. \tag{12}$$

The level of correlation of the lift fluctuation can be characterized by the correlation length,

$$\Lambda \equiv 2\int_0^L R_{LL}(\xi)\mathrm{d}\xi, \tag{13}$$

and the centroid of the correlation function

$$\sigma \equiv \frac{2}{\Lambda}\int_0^L \xi R_{LL}(\xi)\mathrm{d}\xi. \tag{14}$$

The vortex-shedding noise is now modeled by the relation[53]

$$I = \frac{\overline{p'^2}}{\rho c} = \frac{\sin^2\theta}{32c^3R^2}\rho U_\infty^6 C_{L^{rms}}'^2 (St)^2 \Lambda(Z-\sigma). \tag{15}$$

The quantities $C_{L^{rms}}'^2$, $(St)^2$, Λ, and σ can be extracted from a CFD simulation and used in eqn. (15) to estimate the vortex-shedding noise. Computation of $R_{LL}(\xi)$ must take into account the spanwise-periodic boundary conditions applied to the CFD solutions. This is done by fitting the computed correlation function to a functional form proposed by Norberg:[54]

$$R_{LL}(\xi) = \left(1 + \left[\frac{\xi}{C\,\Gamma}\right]^n\right)^{-1}, \quad C = \frac{n}{\pi}\sin\frac{\pi}{n}. \tag{16}$$

The fit is performed over only one quarter of the length of the computational domain so that the influence of the periodic boundary condition on the fit is minimized.

Results for radiated far-field sound are presented in terms of the Sound Pressure Level (SPL) in dB, where

$$SPL \equiv 10\log_{10}\left(\frac{\overline{p'^2}}{20\times 10^{-12}\mathrm{Pa}^2}\right) \quad \mathrm{dB} \tag{17}$$

Results for the predicted SPL at the experimental measurement location using eqn. (15) are given in Table 5 for the SACCARA results and in Table 6 for the OVERFLOW results. These can be compared to the experimental values reported in Table 1. The 2-D SACCARA simulations overpredict the noise at both angles of attack by 7–8 dB using this method. This is due to the assumption of perfectly correlated vortex shedding as well as the stronger lift fluctuation predicted by the 2-D simulations. The three-dimensional SACCARA results over-predict the SPL by 3–4 dB, keeping in mind that the experimental value for the tripped case may be higher than the reported free-transition value at $\alpha = 4^\circ$. The longer-span, lower-resolution case ($8h/64$) at $\alpha = 4^\circ$ predicts a lower value than experiment due to a much-less correlated spanwise lift fluctuation.

The OVERFLOW predictions of SPL using Equation (15) without the splitter plate are lower than the SACCARA results, due mainly to a less correlated vortex structure, as indicated by the lower correlation lengths. The value of 95.2 dB at $\alpha = 10^\circ$ is very close to the experimental value of 93.5 dB at $\alpha = 11^\circ$. The splitter plate reduces the noise for $\alpha = 10^\circ$, in accordance with the experimental trend, but underpredicts the amount of reduction by about 7 dB. The simulation actually predicts an increase in noise due to the splitter plate for $\alpha = 4^\circ$; more analysis is required to determine the cause of this increase.

The OVERFLOW surface pressure time histories were also analyzed by the aeroacoustic analysis software PSU–WOPWOP[55–57] to predict the noise generation at the specified observer location. PSU-WOPWOP takes as input the time-dependent surface pressure over the airfoil. It then integrates from the source points to the observer to predict the net noise level. For comparison to the full-span experimental results, the limited-span WOPWOP results were corrected by multiplying the intensity of the sound by the square of

the ratio of the full-span to the limited span. In addition to the surface pressure, wake flow noise can also be included in the analysis. This will be reported in the future. The resulting sound-pressure-levels (SPL) for the two 3-D 10° GT–HRLES OVERFLOW cases are shown in Fig. 9. There, the for the flat-back geometry, the peak sound level is predicted at $St = 0.184$, the same as the dominant vortex shedding mode. The maximum predicted noise generated is approximately 94 dB, within 1.5 dB of the result using the approximate theory of eqn. (15). With the inclusion of the splitter-plate, the peak frequency is shifted to $St = 0.17$ and the maximum sound level is reduced by approximately 4 dB to 89.7 dB, which is very close to the 90.5 dB estimated using eqn. (15). As with the flatback geometry, the peak SPL correlates to the vortex shedding mode. Overall, the PSU–WOPWOP results described above compare well to the theoretical results reported in Table 6, providing a verification of the applicability of the theory.

Table 5. Aeroacoustic noise estimates for SACCARA.

α (deg)	Splitter Plate	Grid	SPL (dB)	Λ/h	σ/h
4	No	2D	101.7	–	–
4	No	$2h/64$	98.4	38.9	9.9
4	No	$4h/64$	98.6	34.1	9.3
4	No	$8h/64$	89.9	15.6	6.3
10	No	2D	101.4	–	–
10	No	$4h/64$	96.5	35.8	9.5

Table 6. Aeroacoustic noise estimate for OVERFLOW with GT–HRLES.

α (deg)	Splitter Plate	Grid	SPL (dB)	Λ/h	σ/h
4	No	OF4d	84.5	11.8	5.5
4	Yes	OF4f	87.2	14.3	6.2
10	No	OF10d	95.2	26.9	8.3
10	Yes	OF10f	90.5	28.2	8.5

D. 3-D Flow Analysis

The frequency of vortex-shedding was seen to correlate quite closely to the peak noise frequency in the previous section. Further, significant correlation was observed in the sectional lift coefficients (C_l) in the 3-D simulations with the level of correlation dependent upon the span-wise resolution. To investigate this, we have visualized the coherent 3-D flow structures in the airfoil wakes. Following Dubief and Delcayre,[58] one may identify coherent structures through iso-surfaces of the *Q-criterion*. The iso-surfaces of $Q \times (c/U_\infty)^2 = 25.3$ for the six 3-D simulations at 4° are shown in Figs. 10 and 11 for SACCARA SADES and OVERFLOW GT-HRLES results, respectively.

In the SACCARA simulations with a spanwise resolution (δ_z) finer than $h/16$ ($0.1c/16$), there are well-defined 2-D rollers with 3-D braids between these. This is most clearly visible in Figs. 10(b) and (d) where the spanwise extent is $4h$ ($0.4c$) or more. This same flow structure is present in the $2h$ simulation, but it is more difficult to observe. While there are more resolved 3-D turbulent flow structures in these higher resolution cases, the spanwise correlation of C_l reported in Table 15 is higher due to the presence of the coherent 2-D rollers. Lower δ_z resolutions predict more unorganized wake flow patterns with poorly defined rollers. However, based on the shedding frequency and aeroacoustic sound levels, there is evidence of bluff-body vortex shedding in these cases. From this, it appears that the less resolved spanwise instability wavelengths are leading to incoherent vortex shedding for the coarser resolution cases. Note that the more incoherent

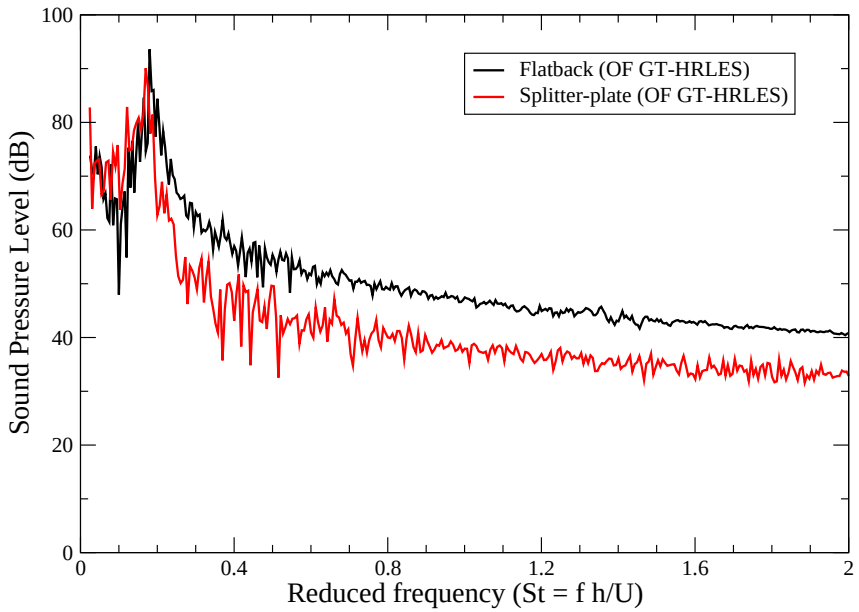

Figure 9. Sound pressure level (SPL) for a 3-D 10° flatback and splitter-plate airfoil simulations using OVERFLOW with GT–HRLES.

shedding associated with coarser spanwise resolution actually improves agreement with the measured experimental mean drag coefficient. Also note that aerodynamic and aeroacoustic quantities for the $8h/128$ case pictured in Fig. 10 have not been reported because it has not yet reached a statistical steady state. It is not clear which vortex-shedding mode more accurately reflects what is observed in experiment: the more two-dimensional roller with braid structure predicted by the finer resolution cases or the less coherent three-dimensional shedding. Further work is needed to determine if more three-dimensional structure can be induced in the fine-grid cases by, for example, altering the initial conditions.

Comparing the wake features predicted by SACCARA and OVERFLOW show similar wake structures (see Figs. 11(a) and 10(b)). However, the flow structures dissipate more rapidly with OVERFLOW. While the wake resolutions in the near-field are similar, the SACCARA mesh maintains the resolution further downstream which may explain the reduced dissipation. An exact matching of conditions is required to rule out numerical algorithm effects.

The distinction between the wake flow with and without the splitter-plate is difficult to discern in the OVERFLOW GT–HRLES simulations. Both predict a highly incoherent shedding pattern following the description above. Simulations at twice the spanwise resolution (not shown) are currently underway which follow the trend of increased coherence with the observation of 2-D rollers and braids. Statistical analysis of these simulations will be reported in the near future.

VII. Conclusion

Computations of the flatback version of the DU97-W-300 airfoil in two and three dimensions using traditional RANS turbulence models and hybrid RANS/LES turbulence simulation techniques within CFD codes have been accomplished. Several conclusions on the efficacy and future promise on the aerodynamic and aeroacoustic prediction capability of these advanced turbulence methods can be drawn:

- Time-averaged lift prediction is insensitive to grid, domain size, and simulation mode (steady RANS vs. unsteady hybrid RANS/LES), and both RANS and hybrid RANS/LES methods typically predict

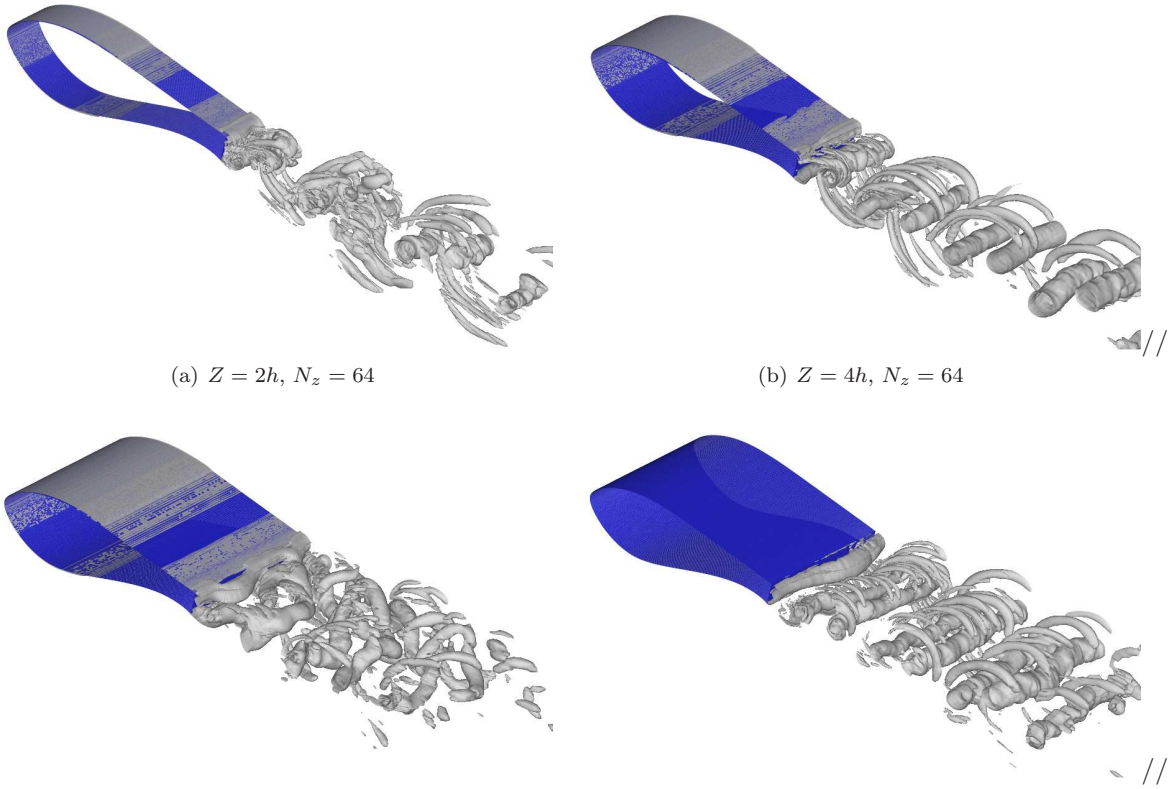

(a) $Z = 2h$, $N_z = 64$

(b) $Z = 4h$, $N_z = 64$

(c) $Z = 8h$, $N_z = 64$

(d) $Z = 8h$, $N_z = 128$

Figure 10. Isosurface of Q from SACCARA at $\alpha = 4°$.

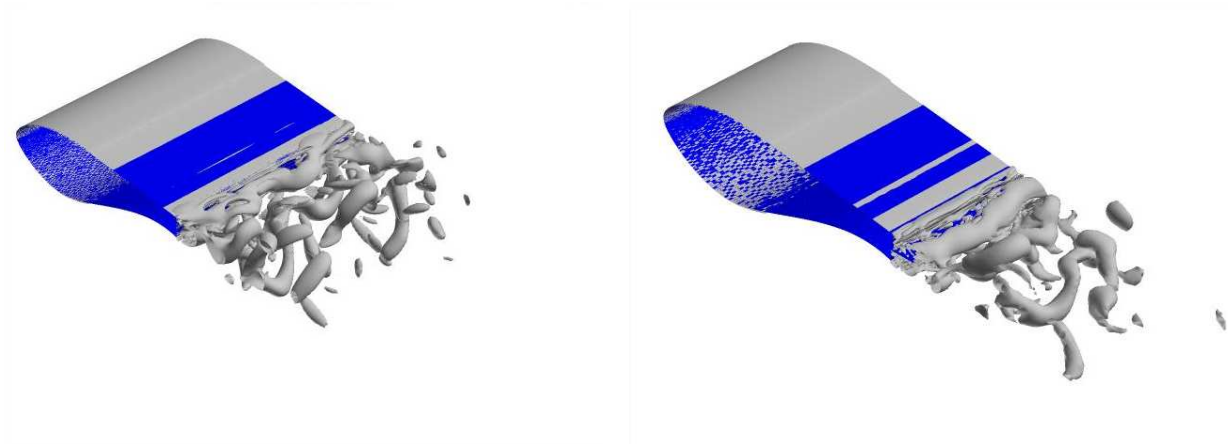

(a) flatback: $Z = 10h$, $N_z = 65$

(b) splitter-plate: $Z = 5h$, $N_z = 33$

Figure 11. OVERFLOW GT-HRLES instantaneous images of Q-criterium iso-scalar ($Q*(c/U_\infty)^2 = 25.3$) surface for $\alpha = 4°$ with (b) and without (a) splitter-plate.

lift coefficients within experimental bounds for the two angles of attack examined (4° and 10°). As the angles of attack are relatively mild with primarily attached flow, significant differences in the lift coefficients predicted by RANS and hybrid RANS/LES are not expected, as noted in prior applications.

- Time-averaged drag is consistently lower and more accurate for RANS than for unsteady hybrid RANS/LES in two dimensions, as expected. The unstructured drag simulations using both RANS and hybrid RANS/LES are the exception to this, as both provide mean drag coefficients that are very close or within experimental bounds. In three-dimensions, while the unsteady simulations predict a lower drag than two-dimensional simulations, further study to provide guidance on grid independency is needed. The improved correlation of the drag on grids with larger spanwise computational domains appears to result from wake structures that have more three-dimensional features.

- For the finest grid SACCARA simulations, The RMS lift fluctuation is highly correlated along the span ($C'_{L^{rms}} \approx C'_{l^{rms}}$) for all unsteady simulations. For $\alpha = 4$ degrees, $C'_{L^{rms}}$ is highest for the two-dimensional simulations and lowest for the simulation on the $0.8c$ (largest computational extent) grid. It decreases for $\alpha = 10$ degrees.

- Strouhal number of the vortex shedding is insensitive to grid resolution, domain size, and angle of attack, but appears to be $10to15\%$ lower than experiment.

- The RMS drag fluctuation is not as highly correlated ($C'_{D^{rms}} < C'_{d^{rms}}$) as the lift fluctuation ($C'_{L^{rms}} \approx C'_{l^{rms}}$) for the SACCARA three-dimensional simulations.

- Aeroacoustic predictions using both approximate theory and integrated surface pressures from the simulations agree well with one another. For the $\alpha = 10°$ case, simulation predictions are within 4 dB of experimental values, with the level of agreement dependent on the grid resolution, domain size, and code used. OVERFLOW predicted a decrease in SPL due to the splitter plate of 5 dB at $\alpha = 10°$.

Acknowledgments

This work was supported in part by the National Science Foundation, Project 0731034, "Advancing Wind Turbine Analysis and Design for Sustainable Energy". The authors would like to thank NSF and the NSF Program Officer, Dr. Trung Van Nguyen, for their support in this endeavor. Additional funding was provided by Sandia National Laboratories, Wind Energy Technology Department, under contract #793065. Sandia is a multiprogram laboratory operated by Sandia Corporation, a Lockheed Martin Company for the United States Department of Energy's National Nuclear Security Administration under contract DE-AC04-94AL85000. Computational support for this research was supported in part by the National Science Foundation through TeraGrid[59] (grant # TG-MSS080017N) and Sandia National Laboratories. TeraGrid resources were provided by NCSA and SDSC.

The authors would like to thank James Erwin at Pennsylvania State University for his aid in obtaining acoustic data from the computations, as well as the FUN3D Development Team for their aid in the FUN3D simulations.

References

[1]Hubbard, H. and Shepherd, K., "Wind turbine acoustics," TP 20320-77, NASA, December 1990.

[2]Hubbard, H. and Shepherd, K., "Aeroacoustics of large wind turbines," *Acoustical Society of America Journal*, Vol. 89, June 1991, pp. 2495–2508.

[3]Migliore, P. and Oerlemans, S., "Wind tunnel aeroacoustic tests of six airfoils for use on small wing turbines," *Journal of Solar Energy Engineering*, Vol. 126, November 2004, pp. 974–985.

[4]Standish, K. and van Dam, C., "Aerodynamic analysis of blunt trailing edge airfoils," *Journal of Solar Energy Engineerging*, Vol. 125, Novemeber 2003, pp. 479–487.

[5]Paquette, J. A. and Veers, P., "Increased Strength in Wind Turbine Blades through Innovative Structural Design," *Proceedings of the European Wind Energy Conference*, 2007.

[6]Berg, D. E. and Zayas, J. R., "Aerodynamic and aeroacoustic properties of flatback airfoils," *AIAA Paper 2008–1455*, 2008.

[7]Baker, J., Mayda, E., and van Dam, C., "Computational and Experimental Analysis of Thick Flatback Wind Turbine Airfoils," *AIAA Paper 2006–0193*, 2006.

[8]Brooks, T. F., Pope, D. S., and Marcolini, M. A., "Airfoil self-noise and prediction," *NASA RP-1218*, 1989.

[9]Sorensen, N. N., Michelsen, J. A., and Schreck, S., "Navier-Stokes Predictions of the NREL Phase VI rotor in the NASA Ames 80ft x 120 ft wind tunnel," *Wind Energy*, Vol. 5, 2002, pp. 151–169.

[10]Duque, E. P. N., Burklund, M. D., and Johnson, W., "Navier-Stokes and Comprehensive Analysis Performance Predictions of the NREL Phase VI Experiment," *Solar Energy Engineering*, Vol. 125, 2003, pp. 457–467.

[11]Strawn, R. C., Caradonna, F., and Duque, E., "30 Years of rotorcraft computational fluid dynamics research and development," *Journal of the American Helicopter Society*, Vol. 51, No. 1, 2006.

[12]Spalart, P. R., Jou, W.-H., Strelets, M., and Allmaras, S. R., "Comments on the Feasibility of LES for Wings and on a Hybrid RANS/LES Approach," *Advances in DNS/LES*, edited by C. Liu and Z. Liu, Greyden Press, 1997, pp. 1–20.

[13]Kim, W.-W. and Menon, S., "A new dynamic one-equation subgrid-scale model for large-eddy simulations," *AIAA Paper 95-0356*, 1995.

[14]Erlebacher, G., Hussaini, M. Y., Speziale, C. G., and Zang, T. A., "Toward the Large-Eddy Simulation of Compressible Turbulent Flows," *Journal of Fluid Mechanics*, Vol. 238, 1992, pp. 155–185.

[15]Ghosal, S., "On the large eddy simulation of turbulent flows in complex geometries," *Center for Turbulence Research: Annual Research Briefs*, 1993, pp. 11–128.

[16]Strelets, M., "Detached eddy simulation of massively separated flows," *AIAA Paper 2001-0879*, 2001.

[17]Smagorinsky, J., "General circulation experiments with the primitive equations," *Monthly Weather Review*, Vol. 91, No. 3, 1993.

[18]Barone, M. and Berg, D., "Aerodynamic and Aeroacoustic Properties of a Flatback Airfoil: An Update," AIAA Paper 2009-0271, 2009 ASME Wind Energy Symposium, 2009.

[19]Baurle, R. A., Tam, C. J., Edwards, J. R., and Hassan, H., "Hybrid Simulation Approach for Cavity Flows: Blending, Algorithm, and Boundary Treatment Issues," *AIAA Journal*, Vol. 41, No. 8, 2003, pp. 1463–1480.

[20]Sanchez-Rocha, M., *Wall-Models for Large Eddy Simulation Based on a Generic Additive- Filter Formulation*, Ph.D. thesis, Georgia Inst. of Technology, 2008.

[21]Wilcox, D., *Turbulence Modeling for CFD*, CDW Industries, La Canada, CA, 2nd ed., 1998.

[22]Sanchez-Rocha, M., Kirtas, M., and Menon, S., "Zonal hybrid RANS–LES method for static and oscillating airfoils and wings," *AIAA Paper 2006-1256*, 2006.

[23]Kok, J., Dol, H., Oskam, B., and van der Ven, H., "Extra large eddy simulations of massively separated flows," *AIAA Paper 2004-0264*, 2004.

[24]Stone, C., Tebo, S. M., and Duque, E., "Computational fluid dynamics of flatback airfoils for wing turbine applications," *AIAA Paper 2006-0194*, 2006.

[25]Lynch, C. E. and Smith, M. J., "Hybrid RANS–LES Turbulence Models on Unstructured Grids," *AIAA Paper 2008–3854*, 2008.

[26]Menter, F., "Two-equation eddy-viscosity turbulence models for engineering applications," *AIAA Journal*, Vol. 32, No. 8, 1994, pp. 598–605.

[27]Smith, M. J., Wong, T.-C., Potsdam, M., Baeder, J., and Phanse, S., "Evaluation of CFD to Determine Two-Dimensional Airfoil Characteristics for Rotorcraft Applications," *Journal of the American Helicopter Society*, Vol. 51, No. 1, 2006.

[28]Shelton, A. B., Braman, K., Smith, M. J., and Menon, S., "Improved Turbulence Modeling for Rotorcraft," *Proceedings of the 62nd American Helicopter Society Annual Forum, Phoenix, AZ, May 9-11,2006*, 2006.

[29]Renaud, T., D. M. O'Brien, J., Smith, M. J., and Potsdam, M., "Evaluation of Isolated Fuselage and Rotor-Fuselage Interaction Using CFD," *Journal of the American Helicopter Society*, Vol. 53, No. 1, 2008, pp. 3–17.

[30]Menon, S. and Kim, W.-W., "A New Dynamic One-Equation Subgrid Model for Large-Eddy Simulations," *AIAA Paper 1995–0352*, 1995.

[31]Speziale, C. G., "Turbulence Modeling for Time Dependent RANS and VLES: A review," *AIAA Journal*, Vol. 36, No. 2, 1998, pp. 173–184.

[32]Timmer, W. and van Rooij, R., "Summary of the Delft University wind turbine dedicated airfoils," *J. Solar Energy Engineering*, Vol. 125, 2003, pp. 488–496.

[33]Berg, D. and Barone, M., "Aerodynamic and Aeroacoustic Properties of a Flatback Airfoil," 2008 AWEA Windpower Conference, 2008.

[34]Wong, C. C., Blottner, F. G., Payne, J. L., and Soetrisno, M., "Implementation of a parallel algorithm for thermo-chemical nonequilibrium flow solutions," AIAA Paper 95-0152, January 1995.

[35]Yee, H. C., "Implicit and Symmetric shock capturing schemes," NASA-TM-89464, May 1987.

[36]Sjögreen, B. and Yee, H., "Multiresolution wavelet based adaptive numerical dissipation control for high order methods," *J. Scientific Computing*, Vol. 20, No. 2, 2004, pp. 211–255.

[37]Spalart, P. R., Jou, W.-H., Strelets, M., and Allmaras, S. R., "Comments on the feasibility of LES for wings, and on a hybrid RANS/LES approach," Advances in DNS/LES, 1st AFOSR International Conference on DNS/LES, Greyden Press, 1997.

[38]Girimaji, S. S., "Partially-Averaged Navier-Stokes model for turbulence: A Reynolds-Averaged Navier-Stokes to Direct Numerical Simulation bridging method," *J. Appl. Mech.*, Vol. 73, 2006, pp. 413–421.

[39]Buning, P., Parks, S., Chan, W., and Renze, K., "Application of the Chimera Overlapped Grid Scheme to Simulation of Space Shuttle Ascent Flows," *Proceedings of the Fourth International Symposium on Computational Fluid Dynamics*, Vol. 1, 1991, pp. 132–137.

[40]Ahmad, J. and Duque, E., "Helicopter rotor blade computation in unsteady flows using moving overset grids," *Journal of Aircraft*, Vol. 33, No. 1, 1996, pp. 54–60.

[41]Meakin, R., "Moving grid overset grid methods for complete aircraft tiltrotor simulations," *AIAA Paper 93-3350*, 1993.

[42]Lim, J. and Strawn, R., "Prediction of HART II rotot BVI loading and wake system using CFD/CSD loose coupling," *AIAA Paper 2007–1281*, 2007.

[43]Duque, E., van Dam, C., and Hughes, S., "Navier-Stokes simulations of the NREL combined experiment Phase II rotor," *AIAA Paper 99-0037*, 1999.

[44]Meakin, R., "Unsteady simulation of the viscous flow about a V-22 rotor and wing in hover," *AIAA Paper 95-3463*, 1995.

[45]Potsdam, M. A., Venkateswaran, S., and Pandya, S., "Unsteady low Mach preconditionging with application to rotorcraft flows," *AIAA Paper 2007-4473*, 2007.

[46]Bonhaus, D., *An Upwind Multigrid Method For Solving Viscous Flows On Unstructured Triangular Meshes*, Masters thesis, George Washington University, 1993.

[47]Anderson, W., Rausch, R., and Bonhaus, D., "Implicit/Multigrid Algorithms for Incompressible Turbulent Flows on Unstructured Grids," *Journal of Computational Physics*, Vol. 128, No. 2, 1996, pp. 391–408.

[48]OBrien, D. M. and Smith, M. J., "Analysis of Rotor-Fuselage Interactions Using Various Rotor Models," *AIAA 43rd Aerospace Sciences Meeting, Reno, NV*, 2005.

[49]Biedron, R., Vatsa, V., and Atkins, H., "Simulation of Unsteady Flows Using an Unstructured Navier-Stokes Solver on Moving and Stationary Grids," *Proceedings of the 23rd AIAA Applied Aerodynamics Conference, Toronto, Canada*, 2005.

[50]Chorin, A., "A Numerical Method for Solving Incompressible Viscous Flow Problems," *Journal of Computational Physics*, Vol. 2, No. 1, 1967, pp. 12–26.

[51]Roe, P., "Approximate Riemann Solvers, Parameter Vectors, and Difference Schemes," *Journal of Computational Physics*, Vol. 43, No. 10, 1981, pp. 357–371.

[52]Kravchenko, A. G. and Moin, P., "Numerical Studies of Flow over a Circular Cylinder at $Re_D = 3900$," *Physics of Fluids*, Vol. 12, No. 2, 2000, pp. 403–417.

[53]Blevins, R., *Flow-Induced Vibration*, Krieger Publishing Company, Malabar, FL, 2nd ed., 2001.

[54]Norberg, C., "Fluctuating Lift on a circular cylinder: review and new measurements," *J. Fluids and Structures*, Vol. 17, 2003, pp. 57–96.

[55]Hennes, C., Lopes, L., Shirey, J., and Erwin, J., "PSU-WOPWOP 3.3.2 User's Guide," Tech. rep., The Pennsylvania State University, 2008.

[56]Hennes, C. and Brentner, K., "The effect of blade flexibility on rotorcraft acoustics," *Proceedings of the 31st European Rotorcraft Forum*, 2005.

[57]Brentner, K. and Farassat, F., "Analytical comparison of the acoustic analogy and kirchoff formulation for moving surfaces," *AIAA Journal*, Vol. 36, No. 8, 1998, pp. 1379–1386.

[58]Dubief, Y. and Delcayre, F., "On coherenent-vortex identification in turbulence," *Journal of Turbulence*, Vol. 1, No. 11, 2000.

[59]Catlett, C., *"TeraGrid*: Analysis of Organization, System Architecture, and Middleware Enabling New Types of Applications," *HPC and Grids in Action, Ed. Lucio Grandinetti, IOS Press 'Advances in Parallel Computing' series, Amsterdam, 2007*, 2007.